Hapke modeling of Rhea surface properties through Cassini-VIMS spectra

M. Ciarniello, F. Capaccioni, G. Filacchione, R.N. Clark, D.P. Cruikshank, P. Cerroni, A. Coradini, R.H. Brown, B.J. Buratti, F. Tosi, et al.

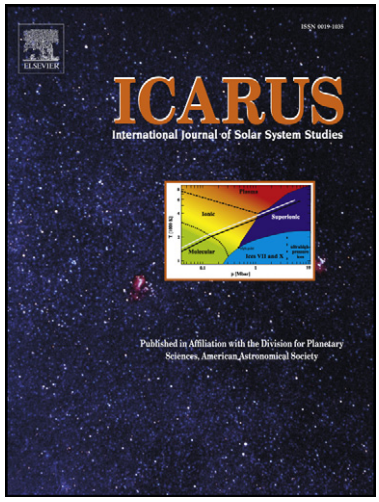

Hapke modeling of Rhea surface properties through Cassini-VIMS spectra

M. Ciarniello, F. Capaccioni, G. Filacchione, R.N. Clark, D.P. Cruikshank, P. Cerroni, A. Coradini, R.H. Brown, B.J. Buratti, F. Tosi, K. Stephan

PII: S0019-1035(11)00175-8
DOI: 10.1016/j.icarus.2011.05.010
Reference: YICAR 9817

To appear in: *Icarus*

Received Date: 18 January 2011
Revised Date: 9 May 2011
Accepted Date: 10 May 2011

Please cite this article as: Ciarniello, M., Capaccioni, F., Filacchione, G., Clark, R.N., Cruikshank, D.P., Cerroni, P., Coradini, A., Brown, R.H., Buratti, B.J., Tosi, F., Stephan, K., Hapke modeling of Rhea surface properties through Cassini-VIMS spectra, *Icarus* (2011), doi: 10.1016/j.icarus.2011.05.010

Hapke modeling of Rhea surface properties through Cassini-VIMS spectra

M. Ciarniello[1*], F. Capaccioni[1], G. Filacchione[1], R. N. Clark[2], D. P. Cruikshank[3], P. Cerroni[1], A. Coradini[4], R. H. Brown[5], B. J. Buratti[6], F. Tosi[4], K. Stephan[7]

[1]INAF-IASF, via del Fosso del Cavaliere, 100, Rome, Italy

[2]U.S. Geological Survey, Federal Center, Denver, CO 80225 USA

[3]NASA Ames Research Center, Moffett Field, CA 94035 USA

[4]INAF-IFSI, via del Fosso del Cavaliere, 100, Rome, Italy

[5]Lunar and Planetary Lab and Steward Observatory, University of Arizona, Tucson, AZ 85721 USA

[6]Jet Propulsion Laboratory, California Institute of Technology, Pasadena, CA 91109 USA

[7]Institute for Planetary Exploration, DLR, Berlin, Germany

Manuscript Pages: 43

Number of Tables: 4

Number of Figures: 12

Proposed Running Head: Hapke modeling of Rhea surface properties through Cassini-VIMS spectra

***Corresponding author:** Mauro Ciarniello

INAF-IASF Istituto di Astrofisica Spaziale e Fisica Cosmica

Via del Fosso del Cavaliere, 100, 00133 Rome, Italy

Phone: (0039)(06) 45488689

Email: mauro.ciarniello@iasf-roma.inaf.it

Abstract

The surface properties of the icy bodies in the saturnian system have been investigated by means of the CASSINI- VIMS (Visual Infrared Mapping Spectrometer) hyperspectral imager which operates in the 0.35-5.1 μm wavelength range. In particular, we have analyzed 111 full disk hyperspectral images of Rhea ranging in solar phase between 0.08° and 109.8°. These data have been previously analyzed by Filacchione et al. (2007, 2010) to study, adopting various "spectral indicators" (such as spectral slopes, band depth, continuum level, etc.), the relations among various saturnian satellites. As a further step we proceed in this paper to a quantitative evaluation of the physical parameters determining the spectrophotometric properties of Rhea's surface. To do this we have applied Hapke

(1993) IMSA model (Isotropic Multiple Scattering Approximation) which allow us to model the phase function at VIS-IR (visible-infrared) wavelengths as well as the spectra taking into account various types of mixtures of surface materials. Thanks to this method we have been able to constrain the size of water ice particles covering the surface, the amount of organic contaminants, the large scale surface roughness and the opposition effect surge. From our analysis it appears that wavelength dependent parameters, e.g. opposition surge width (h) and single-particle phase function parameters (b,v), are strongly correlated to the estimated single-scattering albedo of particles. For Rhea the best fit solution is obtained by assuming:1) an intraparticle mixture of crystalline water ice and a small amount (0.4%) of Triton tholin; 2) a monodisperse grain size distribution having a particle diameter a_m= 38 μm; and 3) a surface roughness parameter value of 33°. The study of phase function shows that both Shadow Hiding and Coherent Backscattering contribute to the opposition surge. This study represents the first attempt, in the case of Rhea, to join the spectral and the photometric analysis. The surface model we derived gives a good quantitative description of both spectrum and phase curve of the satellite. The same approach and model, with appropriate modifications, shall be applied to VIMS data of the other icy satellites of Saturn, in order to reveal similarities and differences in the surface characteristics to understand how these bodies interact with their environment.

1. Introduction and Rationale

The Cassini spacecraft completed its initial four-year mission to explore the saturnian system in June 2008. Since then it entered in the extended mission phase (*Cassini-Huygens Equinox Mission*), which will last until September 2010. During all these years the VIMS (Visual and Infrared Mapping Spectrometer) instrument on board Cassini extensively observed the saturnian moons. The VIMS experiment consists of two imaging spectrometers observing the same field of view in two spectral ranges (Brown et al., 2004; McCord et al., 2004): VIMS-V spectrometer covering the 0.35 - 1.05 μm range in 96 spectral channels with a spectral sampling of $\Delta\lambda$ = 7.3 nm/band and spatial

resolutions of 500×500 (nominal) or 166×166 (high resolution) μrad×μrad /pixel; VIMS-IR channel covering the 0.885 - 5.1 μm range with 256 bands, a spectral sampling of $\Delta\lambda \approx 16$ nm/band and spatial resolutions of 500×500 (nominal) or 250×500 (high resolution) μrad×μrad /pixel (Miller et al., 1996).

VIMS collected both resolved and disk-integrated spectra of the moons in a wide range of observing conditions (solar phase angle and hemispheric coverage). While high spatial resolution observations of the satellites are essential to obtain compositional maps of the objects, the disk integrated observations are very useful to study the global properties of the surfaces and to point out correlations as well as differences among the various satellites.

The full disk observations constitute of a huge database with more than 1400 observations, obtained over a wide range of phase angles, for a total of 126000 spectra, covering the full VIMS spectral range. For a detailed description of the database see Filacchione et al. (2007, 2010) (in the following referred to as F2007 and F2010 respectively).

Spectrophotometry is a very powerful diagnostic tool in remote sensing to study the composition and the physical properties of the surfaces of objects under investigation. The amount of solar radiation, as a function of the wavelength, scattered from a surface towards the observer under varying observing conditions (incidence, emergence and phase angles) is a nonlinear function of several parameters such as the composition of the materials making up the surface, their grain size, the porosity and surface roughness of the interacting surface layers.

To retrieve quantitative information on these fundamental parameters of the surfaces, we need a multiple scattering model which provide approximate solutions to the radiative transfer in a particulate medium. The Hapke IMSA model (Hapke, 1993, 2002, 2008; Hapke et al. 2009) is one of several models developed to study the scattering properties of packed media (Lumme and Bowell, 1981; Drossart 1993; Shkuratov et al., 1999). It is an analytic two stream approximate

95 solution to the radiative transfer equation and it has been applied successfully to perform
96 photometric corrections of imaging data (Hudson and Ostro, 1999; Domingue et al., 2009), to
97 investigate physical properties of regoliths (Mallama et al., 2002; Buratti et al., 2004) and to
98 estimate surface compositions of planetary surfaces (Cruikshank et al., 2001; Cruikshank et al.,
99 2005; Poulet et al., 2002).

100 In F2007 and F2010 the authors have adopted an empirical method of spectral analysis to reduce the
101 dimensionality of the spectra by mapping high dimensional data into a lower dimension while
102 preserving the main features of the original spectra. This led to the definition of a number of
103 "Spectrophotometric Indicators" which are able to synthetically describe the spectrum. For instance
104 spectral slopes in the visible range are a useful indicator of the degree of purity of water ice with
105 respect to the presence of contaminants, thus two of the selected indicators are the slopes in the blue
106 range of the spectrum (350-550nm) and in the NIR (near infrared) range (550-1000nm). In the IR
107 range the most prominent features are the water ice absorption bands; consequently the authors have
108 selected the depth of the 1.2, 1.5, 2.0 and 3.0μm water ice bands as additional indicators.

109

110 The systematic analysis performed in F2007/F2010 on the basis of these indicators indeed pointed
111 out several compositional trends within the satellites system and raised several questions which
112 have not yet received a satisfactory answer. For instance:

113 • the correlation among Phoebe, Iapetus and Hyperion. The origin of the material that causes
114 the albedo dichotomy of Iapetus has been the subject of a long standing debate (Buratti and
115 Hicks, 2003; Spencer and Denk, 2010; Tosi et al., 2010). However, Clark et al. (2008,
116 2011b), showed that the visible colors and UV absorber are consistent with a single source
117 with varying abundance of the contaminants. Key to solution of the problem was the
118 discovery of Rayleigh scattering from small particles (Clark et al., 2008). From the VIMS

data the spectral behaviour in the VIS-NIR range shows similarities between Iapetus and Hyperion; while the IR spectra point out a strong correlation between the features observed on Iapetus and Phoebe.

- The Band Depth at 1.5 μm versus Band Depth at 2.0 μm trend is the result of the combined effect of ice contamination, due to "darkening agents" as well as variable grain sizes, but the relative contribution of the two effects could not be ascertained. However, Clark et al. (2011a, 2011b) show that the 1.5 and 2.0 μm ice band depth ratio is affected by the amount of sub-micron sized ice grains in the regolith.

- The symmetry of the 2-micron ice bands is unusual, being asymmetric toward longer wavelengths in spectra of the icy saturnian satellites (Clark et al., 2008) and in other icy objects (see review by Clark et al., 2011a). Clark et al., (2010b) showed that this asymmetry could be due to the presence of sub-micron ice grains and modelled the spectra using Hapke theory modified to include the diffraction component from those particles.

From this point of view the analysis performed in F2007 and F2010 represent a valuable empirical study to describe the global properties of the surfaces of the moons, however quantitative estimates on the nature (composition and physical properties) of the regolith require a full radiative transfer model. We have then set ourselves to work to this task (Ciarniello et al., 2010a, 2010b), and this paper describes the results we have obtained applying a radiative transfer model to the complete data set of Rhea's full disk observations.

Rhea, with a radius of 764 ± 1.1 km (Thomas et al., 2006), is the second largest moon of Saturn; it orbits in the E ring with mean semimajor axis of 527070 km (see http://ssd.jpl.nasa.gov and reference therein); its mass is M = (2.306481 ± 0.000059)x10^{21} kg, which corresponds to a density

of 1232.8 ± 5.4 kgm^{-3} (Iess et al., 2007) and geometric albedo of the satellite is 0.83 at 0.51 μm (Pitman et al., 2010).

We have selected Rhea as the starting point for this analysis as it has the largest coverage in solar phase angle and thus allows to thoroughly test the model. Our approach is based on a two steps analysis: first a spectral fit is performed to retrieve the abundances of contaminants and ice grain size, then these properties are used to compute single-scattering albedo at each wavelength, whose values are adopted in the Rhea's phase function fit for the whole VIMS spectral range.

In section 2 we have described the method applied to model the phase curves and the spectra. In section 3 the selected dataset is described as well as the reduction data procedure. In sections 4 and 5 spectral and phase function fits respectively are analyzed. Section 6 concerns the feedback of phase function fit to the spectrum fit. Conclusions and suggested future work are given in section 7.

.

2. Hapke model

Hapke's IMSA (Isotropic Multiple Scattering Approximation) model has been widely used to describe both solar phase curve and spectral properties of various objects in the solar system (Buratti 1985; Bowell et al. 1989; Domingue et al. 1995; Domingue and Verbiscer 1997). In this paper we refer to Hapke (1993) in order to describe the spectrophotometric properties of Rhea. For our analysis we have chosen full-disk images of the satellite and the formula we applied to describe the object full disk reflectance (FDR) as a function of the phase angle g is straightforward derived by Eq. 10.40, p.275 in Hapke (1993):

$$FDR(g) = \int_{A(i,v)} r(i,e,g)S(i,e,g)\mu d\Omega = \left\{\frac{1}{8}\left\{1-\sin(\tfrac{g}{2})\tan(\tfrac{g}{2})\ln[\cot(\tfrac{g}{4})]\right\}\left\{[(1+B(g))p(g)-1]w+4r_0(1-r_0)\right\}+ \right.$$
$$\left. +\frac{4}{3}r_0^{\,2}\left[\frac{\sin(g)+(\pi-g)\cos(g)}{2\pi}\right]\right\}K(g,\bar{\theta})$$

165

166 (1.)

167 where $r_0 = (1-\gamma)/(1+\gamma)$ and $\gamma = \sqrt{1-w}$.

168 The effect of porosity, which has been introduced in Hapke (2008), is not considered here, similarly
169 to Warell and Davidsson (2010), in order to reduce the number of free parameters in the following
170 inversion process. An improvement of the IMSA model is given in Hapke (2002). It provides a
171 more accurate analytic expression of the Ambartsumian-Chandrasekhar function *H(x)* which
172 appears in the definition of the bidirectional reflectance *r(i,e,g)*. However, we adopted a linear
173 expression for *H(x)* in the derivation of eq. 1 (eq. 8.56, p.212 in Hapke (1993)), since this
174 expression could be easily integrated. Eq. 1 represents the sum of the reflectances *r(i,e,g)* of each
175 point on the surface *A(i,v)*, which is both viewed by the instrument and illuminated by the Sun, as a
176 function of the incidence (*i*), emergence (*e*) and phase (*g*) angles. Each term is weighted by the
177 cosine of the emergence angle μ=*cos(e)* which correctly projects the emitting area on the plane
178 orthogonal to the emission direction, and by the term *S(i,e,g)* which describes the large scale surface
179 roughness (craters, depressions and other reliefs). Two mechanisms contribute to the emission
180 process: single scattering and multiple scattering. The first one depends on the single-particle phase
181 function *p(g)*, which describes how the light interacting with a particle is scattered. Actually the
182 single-particle phase function is an average on a small but statistically significant given volume of
183 particles. We modeled it assuming a double lobed Henyey-Greenstein (Henyey and Greenstein,
184 1941; Domingue and Verbiscer, 1997) phase function (Eq. 2) which depends on two parameters *b*
185 and *v*: the first one describes the angular width of both forward and back scattering lobes, while the
186 second one describes their relative amplitude.

187 $$p(g) = \frac{1+v}{2}\frac{1-b^2}{\left(1-2b\cos g+b^2\right)^{\frac{3}{2}}} + \frac{1-v}{2}\frac{1-b^2}{\left(1+2b\cos g+b^2\right)^{\frac{3}{2}}} \qquad (2)$$

Another term which depends on single scattering is the one that accounts for the opposition effect (OE), $B(g)$. It describes the observed non-linear increase in reflectance towards small phase angles. In this work we use the mathematical formulation developed to treat shadow hiding opposition effect SHOE, which depends on the parameters B_0 and h, respectively the amplitude and the angular width of the effect. Rigorously, B_0 can assume values in the 0-1 range, however we allowed B_0 to be greater than 1 in order to take into account coherent backscattering (CB), which is another mechanism contributing to OE (Roush, 1994). We choose not to model explicitly the CBOE to reduce the number of free parameters. The term $K(g, \bar{\theta})$ in (Eq.1) is the full disk correction due to large scale surface roughness. Its value is always less than 1 and decreases with increasing roughness parameter $\bar{\theta}$, which is an average slope of the facets composing the surface.

Spectral information is included in the single-scattering albedo $w(\lambda)$. This parameter represents the fraction of light interacting with the particle (light can be absorbed, scattered or diffracted) that undergoes only scattering. It's value is in the range 0-1 and depends on the medium optical constants n and k (which are respectively the real and the imaginary part of the refractive index $m=n+ik$), and on the grain size. Similarly to the case of single-particle phase function, the value of the single-scattering albedo is an average over a small but statistically significant volume of particles, and it is calculated as the ratio of the scattering and extinction efficiencies Q_S and Q_E. In close-packed particulate media with spherical grains much larger than the wavelength (which is the assumption we made in our analysis) the IMSA model assumes that diffraction is negligible. In that case the extinction efficiency is 1 (the cross section of the particle is equal to the geometrical cross section) and single-scattering albedo is equal to the scattering efficiency Q_S, which can be directly calculated in the Hapke model once that optical constants of end-members, type of mixing and grain size are fixed.

We have investigated three types of mixing: areal, intimate and intraparticle. *Areal mixing* (Fig. 1a) is obtained averaging the reflectance of different patches of surface covered with different materials:

$$r_{tot} = \sum_i p_i r_i \qquad (3)$$

where r_i is the reflectance of i'th component and p_i is the fraction of total surface covered.

Intimate mixing (Fig. 1b) describes a medium in which particles of different composition are mixed together : this kind of mixing is obtained through a weighted average of single-scattering albedos of the different types of grains:

$$w_{tot} = \frac{\sum_i p_i \sigma_i w_i}{\sum_i p_i \sigma_i} \qquad (4)$$

where σ_i is the geometrical cross section of the i'th particle type and p_i is the volume percentage of each component.

Intraparticle mixing (Fig. 1c) describes media in which inclusions of contaminants are embedded in a matrix of different optical properties. This kind of mixing is obtained with the Maxwell-Garnett rule (Maxwell-Garnett, 1904; Mallet et al.2005; Grundy, 2009):

$$\varepsilon_{eff} = \varepsilon_1 + 3\varepsilon_1 p_2 \frac{(\varepsilon_2 - \varepsilon_1)}{[\varepsilon_2 + 2\varepsilon_1 - p_2(\varepsilon_2 - \varepsilon_1)]} \qquad (5)$$

where ε_1 and ε_2 are the complex dielectric constants of the matrix and of the embedded material respectively, p_2 is the fraction of contaminant and ε_{eff} is the effective complex dielectric constant of the particle. The dielectric constant is related to optical constants by the following relation:

$$m = \sqrt{\varepsilon} = n + ik \qquad (6)$$

Once the medium optical constants and particle diameter a_m are fixed it is possible, following Hapke's model, to compute single-scattering albedo w for a given type of particles. We do not report the single-scattering albedo derivation but refer to Hapke (1993) for further details and final equations.

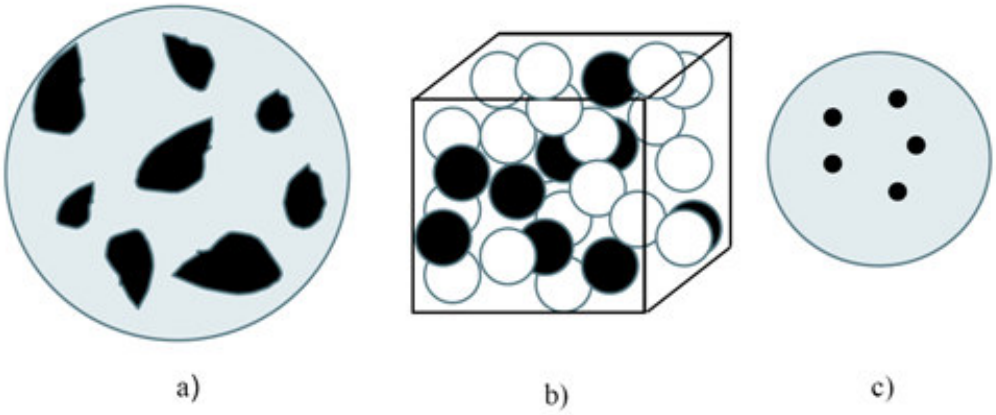

[FIGURE 1]

3. Observations and data reduction

Our dataset is composed of 140 observations acquired by VIMS in the period January 2005 - January 2008. Since Rhea exhibits a marked dichotomy between leading and trailing side (Verbiscer and Veverka, 1989; Buratti et al., 1998) we have selected only images in which the illuminated and observed area was more than 60% on the leading side, in order to study homogeneous regions of the satellite. With this limitation the total number of observations reduces to 111 with solar phase angles ranging from 0.08° to 109.8°.

VIMS collected full disk images of the satellite acquired at different spacecraft-target distance D both in normal and high-resolution modes. Accordingly, the satellite image size in the instrument

field of view can cover from a few tens to some hundreds of pixels. In order to produce phase function curves of the satellite at each wavelength we developed an IDL procedure that sums up the reflectances (I/F) of observed-illuminated pixels in the image, correcting them by the multiplicative factor $\delta\varepsilon D^2 / R^2$ (where R is Rhea's radius and $\delta\varepsilon$ is the solid angle subtended by the pixel). This factor represents the solid angle increment on the satellite surface times the emission angle cosine. The relation between observed data and FDR is:

$$\int_{A(i,v)} r(i,e,g)S(i,e,g)\mu d\Omega \approx \sum_j \left(\frac{I}{F}\right)_j \frac{\delta\varepsilon D^2}{R^2} \qquad (7)$$

where the subscript j identifies each single pixel.

In Fig. 2 Rhea full-disk normalized spectra acquired at various phase angle are plotted (for VIMS calibration uncertainties please refer to McCord et al. (2004)). All the spectra exhibit typical features of water ice (1.51,2.2 and 3.1 μm absorption bands), however towards the UV region the shape of the spectrum strongly departs from the flat behavior of water ice producing a strong reddening. This feature has been traditionally assigned to the presence of organic contaminants as suggested by Cruikshank et al. (1998) and Poulet et al. (2002). However there is no clear additional signature in the IR, and this constrains the amount of contaminants to be at most few percent (Clark and Owensby, 1981). Clark et al., 2008 gave alternative explanations, including UV absorption by other compounds and very small grains (nano-phase) of opaque minerals such as hematite. Clark et al., (2011b) model the shape of the UV absorber with combinations of metallic iron (both large grained and nano-sized particles) and nano-phase hematite. A feature centered at 0.9 μm is present in all the spectra. This seems to be an artifact due to the data calibration process. However, the presence of this feature does not affect the global slope in VIS-IR region and doesn't introduce any offset between the two channels, and thus does not alter the results of the following analysis. The spectra show a certain dependence on observing geometry. The slope in VIS-NIR (around 1 μm) region and the band depth at 1.5 and 2.2 μm slowly increase with increasing phase angle, while this

trend is reversed at 3.5 µm. This peculiar behavior can be partially explained by varying the relative contributions of single and multiple scattering at different wavelengths (related to different values of the single-scattering albedo *w* as we will discuss later) and to a variation of single-particle phase function along the spectrum (even in this case related to *w*).

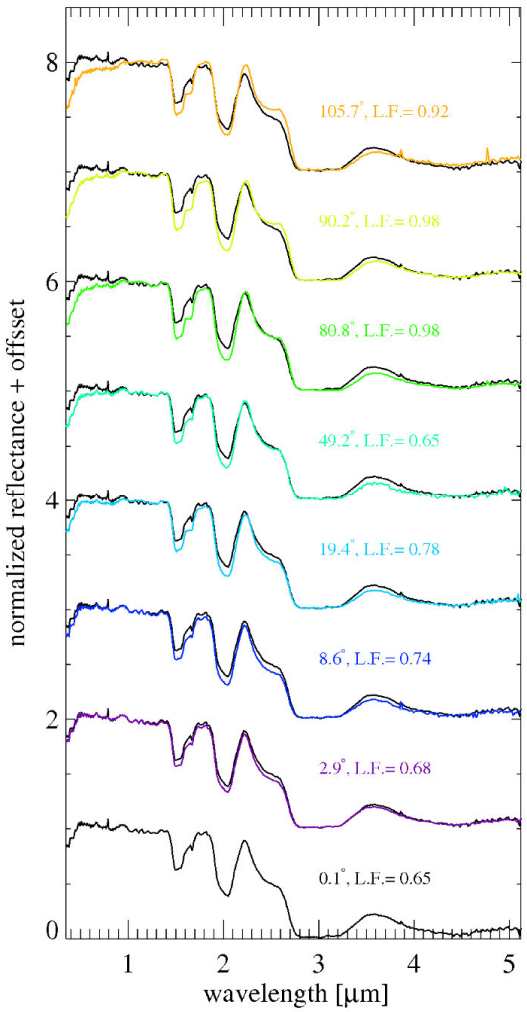

[FIGURE 2]

In Fig. 3 Rhea's normalized full-disk phase functions at various wavelengths are plotted. The coverage is fairly complete across the whole range, except for the 20°-40° region. The shape of the phase function is not constant with wavelength, which is obvious considering the dependence of the spectrum on phase angle mentioned above. In particular, the OE width and reflectance at

intermediate phase angles show a lot of variability while the differences decrease towards larger phase angles.

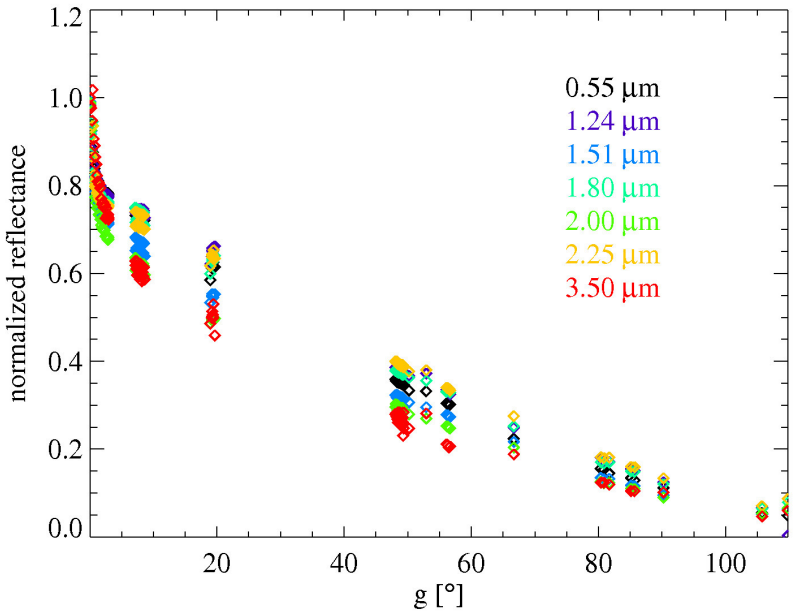

[FIGURE 3]

4. Spectral fit

The first step of our investigation is the interpretation of Rhea spectra in terms of physical characteristics of the surface involved in the scattering process. The principal properties that determine the observed spectral shapes are the composition (in this case water ice + contaminants) and the grain size. The presence of certain end-members is directly correlated with spectral signatures (absorption bands), while the grain size basically affects the depth of the bands as well as the IR slope (Clark and Lucey, 1984; Emery et al., 2005). In Hapke's model the spectral behavior is described by the single-scattering albedo *w*, whose value at each wavelength can be calculated once the end-members, their relative abundances, mixing mode and grain size distribution have been fixed. The single-scattering albedo cannot be directly compared to the observed spectra, because the

295 reflectance at each wavelength depends on single scattering, which relies on the single-particle
296 phase function, and multiple scattering, which involves *w* in a non linear way, as shown in (Eq.1).
297 Moreover, at low phase angle OE must be taken into account, while at high phase angles large scale
298 surface roughness decrease the reflectance.

299 We have chosen to model Rhea's surface by means of a mixture of crystalline water ice and one
300 organic contaminant. We used separately tholin from Khare et al. (1993), Triton tholin (McDonald
301 et al., 1994; optical constants from Cruikshank, personal communication), Titan tholin (McDonald
302 et al., 1994; Khare et al., 1984; optical constants from Cruikshank, personal communication) and
303 hydrogenated amorphous carbon (ACH2) from Zubko et al. (1996). Optical constants for crystalline
304 water ice are those derived by Warren (1984) (0.35-1.25 μm, 266.15 K), Mastrapa et al. (2008)
305 (1.25-2.5 μm, 120 K), Mastrapa et al..(2009) (2.5-3.20 μm, 120 K) and Clark et al. (20110b) (3.20-
306 5.12 μm, 120 K). We investigated areal mixing, intimate mixing and intraparticle mixing. In order
307 to investigate spectral behavior of different mixtures without superimposing any grain size effect
308 we studied only monodisperse particle diameter distribution (particles are all equal in size). This
309 may lead to a non-unique solution, but as we shall see, provides information on the single particle
310 phase function as a function of single particle albedo.

311 The other parameter fixed by the fitting procedure is the volume fraction of water ice *p*, with *pc* =
312 1-*p* being the amount of contaminants.

313 In order to retain a minimum number of parameters we decided to perform the spectral fit at high
314 phase angle (90°) thus avoiding the OE surge. To remove the contribution of large scale surface
315 roughness *K* we fitted normalized spectra (normalization was performed at 1 μm). This choice also
316 allows to minimize the geometrical effects of single-particle phase function which at this stage is
317 assumed isotropic, but may further reduce the uniqueness of the solution.

318 4.1 Optical constants

Summary plots of optical constants Vs wavelength used in this work are shown in Fig. 4-5. In the VIS-NIR range optical constants from Warren et al. (1984) pertain to ice at -7 °C, whose temperature is too high if compared to Rhea's surface at 77 K (Pitman et al., 2010). However these values match reasonably well with the ones derived by Mastrapa et al. (2008) at 120 K. Optical constants in the 3.2-5.1 μm range are from Clark et al. (2011b) and have been computed starting from Mastrapa's values at the same wavelengths. The temperature difference between Rhea's surface and ice for which optical constants are determined introduces a tolerable error in our calculations, because it only minimally affects the results concerning grain size and contamination. The organic compounds, listed above, used to contaminate water ice, all have the effect of producing a red spectrum towards the UV (Fig. 5). Tholin from Khare et al. (1993) have been produced by plasma irradiation in an iced 6:1 mixture of H_2O and C_2H_6 at 77 K. Titan and Triton tholin are instead obtained in gaseous phase by irradiation of 0.9:0.1 and 0.999:0.001 N_2\CH_4 mixtures. ACH2 is obtained by arc discharge between carbon electrodes in H_2 atmosphere.

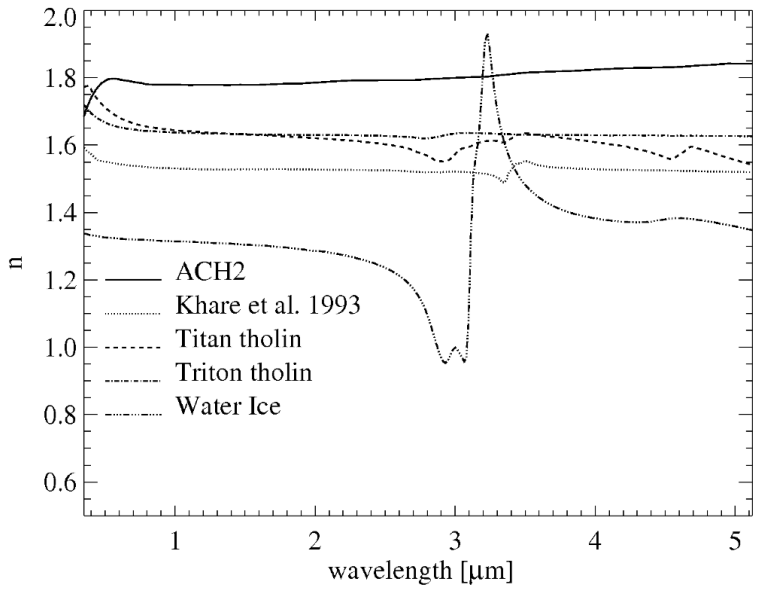

[FIGURE 4]

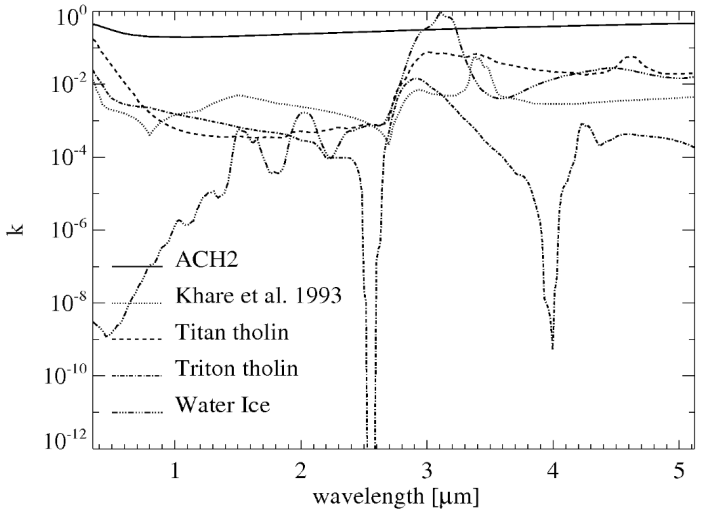

334

335 **[FIGURE 5]**

336

337

338 4.2 Areal mixing

339 We fitted observed spectra with different areal mixtures of two components where the main end-
340 member is always water ice and the second is one among the selected organic contaminants. In
341 areal mixing, the two different types of surface are characterized by different single-scattering
342 albedo, and a beam of light interacts only with particles of the same composition. The resulting
343 spectrum is a linearly-weighted average of the reflectances relative to the different regions. This
344 kind of mixing is inefficient to produce the observed reddening towards UV. As an example we
345 examine the cases of ACH2 and tholin (Khare et al., 1993). In the case of ACH2 the problem is
346 mainly due to the fact that contaminant spectrum is not red enough to produce a sensible effect. It
347 just reduces the reflectance across the whole spectrum without producing any absorption in the UV
348 region, where water ice is strongly non-absorbing. In the normalized spectra this corresponds to an
349 increment of reflectance of the darker wavelengths. This is shown in Fig. 6 (left panel) where the

results of five simulations with different abundances of ACH2 are plotted. The case of tholins (Fig. 6, right panel) is different because their spectra are not as flat as ACH2 far from UV region. In order to produce an effective feature towards short wavelengths many unobserved features are introduced in other regions of the spectrum. The outcome of this simulation is that the strong UV downturn observed in the Rhea spectrum it is not compatible with mixtures including compounds expected to be found on its surface. As an example, the best fit obtained with an areal mixture of water ice and Titan tholin is plotted in Fig. 7 (upper left panel). The results are similar using other types of contaminants. The fit, fairly good in IR, is completely lost in UV-VIS where a plateau is formed at the shortest wavelengths, missing the observed spectral downturn. Results for areal mixtures fits are summarized in Table 1.

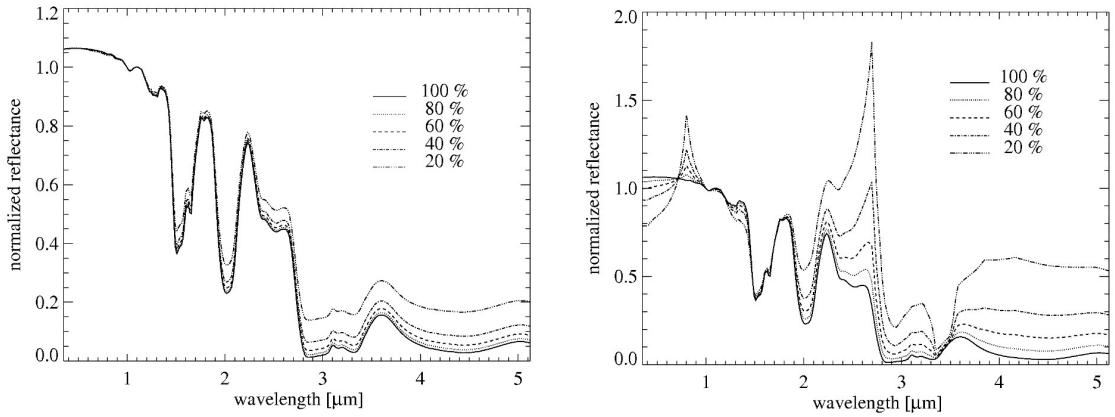

[

FIGURE 6]

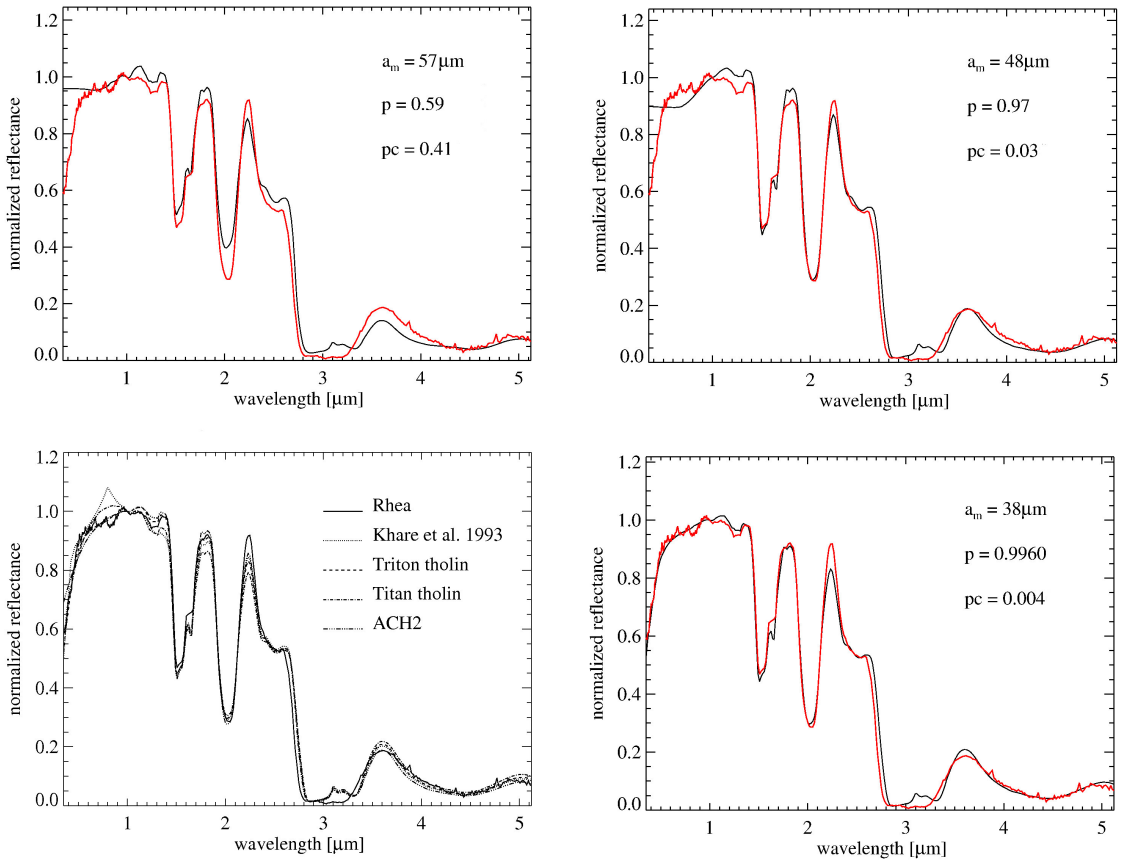

366

367 **[FIGURE 7]**

368

369 **[TABLE I]**

370 4.3 Intimate mixing

371 Similar to the case of areal mixtures we obtained fits to Rhea's spectrum considering intimate
372 mixtures of water ice and the available contaminants. In an intimate mixture, particles of different
373 composition are in close contact (Clark, 1999), so this kind of mixing is also named "salt and
374 pepper" (Poulet et al., 2003). A single ray of light entering the medium in a given position interacts
375 both with water ice particles and contaminant particles. A small volume containing a statistically
376 significant number of particles behaves as if it had an effective single-scattering albedo given by the

377 average of the albedo of the single particles. This kind of mixing is expected to be more efficient
378 than areal mixing because at this stage spectral signatures (e.g. reddening) affect the effective
379 single-scattering albedo and are stretched in higher order terms (w^2, w^3…) involved in the resulting
380 reflectance, while in the case of areal mixtures, spectra of contaminants are only linearly combined.
381 As a result, in intimate mixing, the darker component dominates the spectra signature (Clark, 1999).
382 However, intimate mixing alone is still unable to reproduce the observed reddening of Rhea's
383 spectrum for all the contaminants analyzed. Fig. 7 (upper right panel) shows the best fit obtained
384 with an intimate mixture of water ice and Titan tholin. As with the result of the areal mixture the fit
385 is acceptable in the IR but no reddening is produced towards the UV. The results of the fits are
386 summarized in Table 2.

387

388 **[TABLE II]**

389

390 4.4 Intraparticle mixing

391 In this approach we consider the surface covered by identical particles of water ice with small
392 inclusion of contaminants. The single particle behaves as if it had effective optical constants derived
393 from a combination, given by the Maxwell-Garnett equation, of optical constants of ice and
394 inclusions. For small amount of contaminants (which is the case of this work) the Maxwell-Garnett
395 equation gives results similar to those obtained by a weighted average of the optical constants
396 (Cuzzi and Estrada, 1998). This kind of mixing is the most efficient means of producing reddening
397 because it exaggerates spectral differences, working directly with the complex refractive indices. As
398 shown in Fig. 7 (bottom left panel), intraparticle mixing produces the required UV reddening with
399 every contaminant considered in this work, although the type of reddening change from one
400 contaminant to another. Extremely low concentrations of ACH2 (0.01%) are able to introduce UV

401 reddening, but the resulting spectrum falls too quickly towards short wavelengths before 1 µm and
402 it is not steep enough below 0.4 µm. Titan tholin produces good fits at the shortest wavelengths but
403 it is not sufficiently absorbing towards 1 µm. Tholin from Khare et al. (1993) shows a good
404 agreement below 0.5 µm but has an unobserved feature at 0.8 µm. The best fit (Fig. 7, bottom right
405 panel) is obtained with Triton tholin which reproduces even the change of slope in the spectrum
406 around 0.5 µm. The particle size varies depending on the chosen contaminant. However, if we
407 discard the results given by Titan tholin which produces the worst fit in the IR where the spectrum
408 is more sensitive to grain size, we find that the particles diameter is limited to the range 40-50 µm.
409 This diameter can be considered as an average size of particles, once we assume a monodisperse
410 grain size distribution. Some discrepancies between the final fit and observed spectrum due to
411 particle size are discussed in the next section where the best spectral fit is shown. Results for
412 intraparticle mixtures fits are summarized in Table 3.

413 **[TABLE III]**

414 4.5 Best spectral fit

415 Considering the results presented in previous sections the best way to reproduce the spectral
416 properties of Rhea is to assume an intraparticle mixture of 99.60±0.05 % water ice and 0.40±0.05 %
417 Triton tholin, with a grain diameter of 38.0±0.5 µm (Fig. 7, bottom right panel). Uncertainty on the
418 derived values is related to the procedure we applied to perform the fit, as explained in Appendix
419 A. Despite the small number of free parameters and end-members, the simulated spectrum fits well
420 the observed spectrum. With such a low amount of tholin as a contaminant in the ice, other tholin
421 absorption bands have a small effect on the infrared spectrum where ice is more absorbing. VIS
422 reddening as well as water ice bands are very well reproduced. The secondary absorption band of
423 crystalline water ice at 1.65 µm, which is shown in simulated spectrum, cannot be confirmed in
424 VIMS data because in the wavelength range 1.60-1.66 µm the measured signal is affected by the
425 presence of an order sorting filter on the detector. Consequently, the measured signal in that region

426 is replaced by an interpolated value. One of the stronger discrepancies is in the peak at 2.2 μm. This
427 problem is shown in all the mixtures that have been analyzed so does not depend on the spectral
428 properties of the contaminant but is instead most probably due to the chosen grain size distribution.
429 In the case of monodisperse grain size distribution all the particles are equal and the contribution
430 from smaller particles (with particle size similar or smaller than the wavelength), which certainly
431 are present in a real distribution of sizes, is not considered. It must be noted that Hapke's model is
432 developed in the geometric optics domain, so normally does not deal with grain size smaller than
433 the wavelength. Clark et al. (2011b) have extended the Hapke model to include the diffractive
434 scattering and absorption effects from sub-micron particles. Adopting a distribution of sizes which
435 includes smaller particles it might be possible to reproduce the peak at 2.2 μm. Another part of the
436 spectrum where the fit is lost for all the mixtures we deal with, is given by the absorption band at 3
437 μm. In simulated spectra the 3.1 μm Fresnel peak is always visible, while in the measured spectra it
438 completely disappears. The absence of the Fresnel peak cannot be completely attributed to the
439 relative abundance of amorphous versus crystalline ice, as in amorphous ice the Fresnel peak
440 doesn't fully disappear as shown by (Mastrapa et al., 2009). Moreover ground-based telescopic
441 spectra of Rhea also attest to the crystalline nature of H_2O dominating its surface (Cruikshank et al.
442 2005; Emery et al. 2005). The absence of the Fresnel peak in Rhea's spectra (as in the case for the
443 others icy bodies of the saturnian system) is probably due again to a grain size effect. In large
444 particles light at 3 μm is almost completely absorbed, given the high value of k and the longer path
445 that light travels inside the grain. This implies that when we deal with big grains the light scattered
446 by the particles is the one coming from surface reflections (that involves n) and which generates the
447 Fresnel peak. Scattered light from smaller particles is the result of both surface reflection and
448 internal reflection, thus the Fresnel peak is minimized. Since in our analysis the grain size is around
449 40 μm and the contribution from small particles is neglected, the resulting spectrum exhibits an
450 evident peak at 3.1 μm.

An intraparticle mixture of water ice and Triton tholin was adopted in Cruikshank et al. (2005) where a fit of Rhea spectrum was performed applying the Shkuratov model. It is interesting to note that both approaches require a comparable amount of embedded contaminant (0.4% in this work, 0.2% in Cruikshank et al. (2005)) and they both reproduces the reddening in the UV, even if the adopted spectral models and the surface modeling are different. It reinforces the idea that intraparticle mixing is the best approach to explain the UV feature and that Triton tholin is a reasonable candidate as the water ice contaminant.

5. Phase function fit

Results from the spectral fit allow us to determine the mixture (type of contaminant and mixing modality) and the grain size. The knowledge of these two parameters enables us to compute single-scattering albedo *w* which determines the spectral behavior of the observed surface. This quantity is involved in Eq. 1, which in our approach depends on 5 parameters (apart from *w*). The possibility to fix the single-scattering albedo reduces the complexity of phase function fit procedure and allows the decoupling of spectral effect from photometric ones.

A phase function fit at each wavelength available in VIMS range has been performed, using the surface model given by the best spectral fit that is represented by an intraparticle mixture of water ice and Triton tholin (99.6% - 0.04%), with 38 μm grain size. Parameters relative to the OE (B_0, h) are allowed to vary along the spectrum because, as we mention in section 2, we want to take into account the CBOE as well which can depend on wavelength. Even the single-particle phase function (*b,v*) parameters can vary with wavelength because the single-scattering albedo has spectral variation and modifies the scattering properties of the grain. The large-scale surface roughness parameter ($\bar{\theta}$) is constant all over the spectrum because it accounts only for geometric effects due to surface structures. Details on the fit procedure are in Appendix. In Table 4 the best phase function fit variables for each VIMS channel are reported.

As we deal with particles that are in average larger than the wavelength, we do not expect a direct correlation between the values of parameters obtained by the fit and the wavelength itself. On the other hand, the single-scattering albedo, which determines the contribution of scattering in the light extinction process, plays a fundamental role for the photometric properties at a given wavelength. This implies that the estimated parameters should be correlated with the single-scattering albedo rather than with the wavelength.

[TABLE IV]

5.1 Residuals

Fits are performed minimizing the residuals that are calculated for each wavelength following the formula:

$$res = \Sigma\left(\frac{r_i^m - r_i^c}{r_i^m}\right)^2 , \quad (8)$$

where r_i^m is the measured absolute reflectance at *i*'th phase angle while r_i^c is the value computed by the fit procedure (solar spectrum used to calibrate VIMS data is derived from Thekaekara (1973)). This kind of choice aims to give equal weight to the head and the tail of the full-disk phase function. Reconstructed full-disk phase functions for those wavelengths where the albedo is very low are often dominated by noise, and the corresponding fit parameters values are thought to have no physical meaning. Additionally, they produce high residuals because the model is unable to perform a satisfactory fit. For this reason we have considered for the following analysis only wavelengths with well determined full disk phase function and low value of the residuals. We found that for a residual value of 1 the full disk phase function can be considered well reproduced. From this point to the end of the paper we refer only to results relative to residuals lower than 1, unless explicitly written.

In Fig. 8 (upper left panel) fit residuals for each band are plotted against the value of single-scattering albedo computed for the correspondent wavelength. As we can see the accuracy of the fits increases with larger values of the single-scattering albedo. This effect is due to two reasons. The first is that for those wavelengths corresponding to a higher value of *w* the signal to noise ratio is typically higher and reconstructed phase functions are more accurate. The second is that at low values of the single-scattering albedo the dominating process is single scattering. In this regime the full-disk phase function is more sensitive to single-particle phase function and worse regression accuracy indicates that the Heyney-Greenstein expression is not able to completely describe the scattering process.

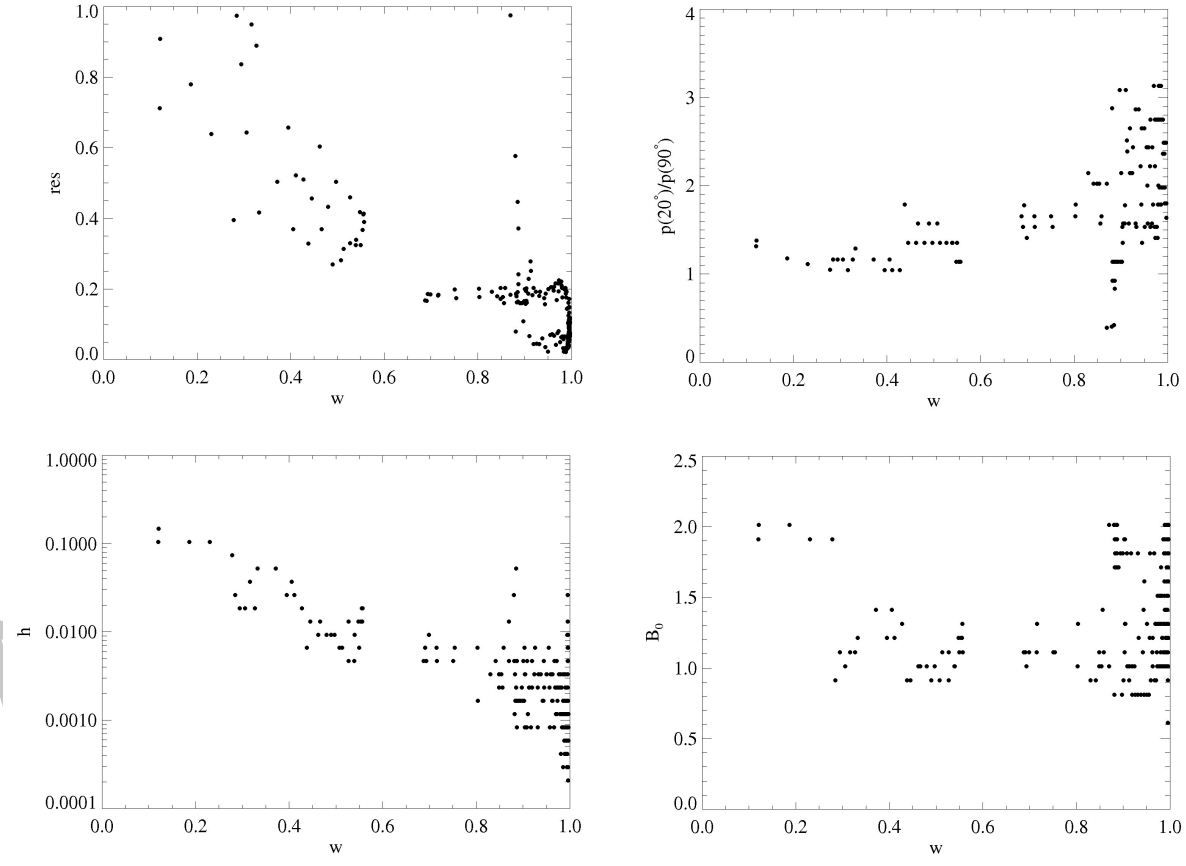

FIGURE 8]

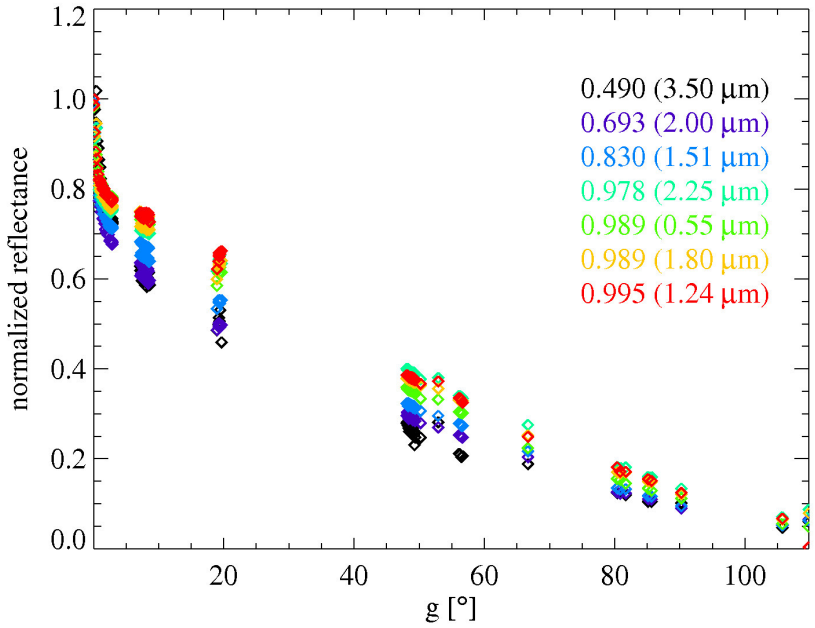

509

510 **[FIGURE 9]**

511

512 5.2 Single-particle phase function

513 In fig.10 the distributions of *b* and *v* parameters are plotted. In these graphs it is shown how many
514 times a certain value of the parameter occurs in a given range of *w* values. According to McGuire
515 and Hapke (1995) a clear spherical particle should have b~ 0.5-0.7 and v~ -0.9. Most of our *b*
516 values are slightly lower (0.3-0.4) as it's expected for real grains that are not perfectly spherical.
517 Moreover *b* values should decrease with increasing absorption and it is what we found, since the
518 fitted values shows a positive correlation with *w*. Concerning the *v* values, they are negative for a
519 large part but greater than -0.9 (average value is -0.5), again as expected for not perfectly spherical
520 particles.

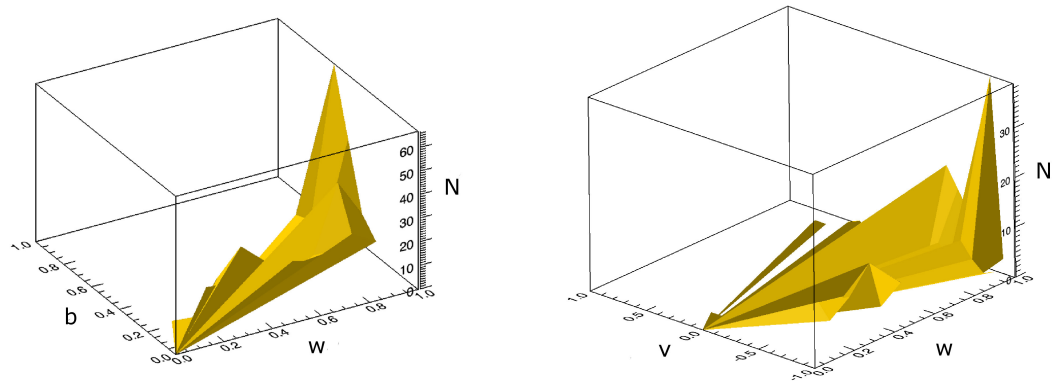

[FIGURE 10]

In order to show any relation between single-particle phase function and single-scattering albedo is useful to investigate the final shape of *p(g)*. In Fig. 8 (upper right panel), the ratio *p(20°)/p(90°)* vs *w* is shown. This choice aims to point out the trend of the single-particle phase function at intermediate phase angles, avoiding the phase angle regions where the contribution of the OE and large scale roughness become relevant. The *p(20°)/p(90°)* ratio increases with single-scattering albedo meaning that reflectance increases at intermediate phase angles (10°-60°) for more transparent particles. This behavior can be explained by the possibility for a light ray to undergo multiple internal reflections in a non-absorbing particle, producing an higher backscattering lobe respect to a darker particle, where surface reflection dominates and produces a quite flat single-particle phase function at phases < 90° (Hapke, 1993, p. 77, Fig. 5.7a). This result is better shown in

Fig. 9, where normalized full disk phase functions are plotted ordered according to increasing values of single-scattering albedo (listed along with their relative wavelengths).

5.3 Opposition effect

As anticipated in previous sections we choose to model the opposition effect following the results developed in Hapke (1993) which consider only shadow hiding (SHOE). This model depends on two parameters (B_0, h) which describes respectively the amplitude and angular width. Nonetheless, another mechanisms, coherent backscattering opposition effect (CBOE), has been recognized as contributing to the OE (Hapke et al., 1998; MacKintosh and Sajeev, 1998; Shkuratov et al. 1999b; Hapke, 2002). Given these reasons the interpretation of results concerning the OE is not trivial, because the two parameters (B_0, h) must describe the contributes of both SHOE and CBOE. The two effects have different characteristics that help us discern between them. The major difference is that angular width of SHOE doesn't depend on wavelength, while the CBOE does (MacKintosh and Sajeev 1998; Hapke 2002). The second one is that the SHOE width extends up to 10° or more while the CBOE is limited to a width of 2°-3° at most (Hapke et al. 1998, Shkuratov et al. 1999b). Additionally we must consider that SHOE is a single-scattering effect while the CBOE develops in a multiple-scattering process. Therefore, we expect that the SHOE dominates for wavelengths corresponding to low values of w while the CBOE dominates at wavelengths where w values is close to 1.

Figure 8 (bottom left panel) shows the plot h against w. The values of h spread over almost three orders of magnitude (0.0002-0.14) giving an OE half width $\Delta g \approx 2h$ ranging between 0.01° - 16°, and show a clear correlation with single-scattering albedo. At low values of w we have high h while the opposite is true when the albedo is low. This behavior reveals the presence of two competing

562 mechanisms in the OE: the CBOE for wavelengths with high value of albedo and the SHOE for the
563 opposite case. This fact agrees with the argument that the CBOE depends on multiple scattering and
564 the SHOE on single scattering. Moreover, we would expect that the *h* values at low *w* would be
565 nearly constants, since SH is independent of wavelength. What we see, in fact, is that spreading
566 reduces considerably towards small values of *w* with *h* approaching 0.1.

567 In the SH regime a rough estimation of the porosity of water ice particles on the surface can be
568 computed from the following relation (Hapke 1993):

569 $$h \approx -\frac{3}{8}\ln(1-\phi) \quad (9)$$

570 where ϕ is the filling factor. The value of *h* we chose to use is 0.1, which is referred to low values
571 of the single-scattering albedo, where single scattering dominate and the OE is due to SH. Moreover
572 this value is almost constant with *w*, so it is independent of wavelength, which is what we expect
573 for the SHOE. With this choice we obtain ϕ =0.23. However, considering that a real grain size
574 distribution has a non null dispersion and that the particle diameter we have measured is just an
575 average value the filling factor can be higher. Assuming a grain size distribution of the form:

576 $$N(a) \propto a e^{-\frac{a}{a_m}} \quad (10)$$

577 we obtain Φ=0.35. The derived porosity is then in the range 65-77 %. These values are lower than
578 those derived in a similar study by Domingue et al. (1995). It must be noted that in Domingue's
579 work the analysis was performed at 0.47 and 0.55 μm, where the single-scattering albedo is close to
580 1 and the CBOE contribution is important, reducing *h* and increasing the estimated porosity.

581 Regarding the amplitude of the opposition effect B_0 (Fig. 8, bottom right panel) we do not find any
582 particular trend with *w,* apart from the fact that values have a larger spreading for single-scattering

albedo close to 1 tending to be higher respect to the rest of the spectrum. This could be an indication of the superimposition of the CB on SH, but a compensating effect due to the unsatisfactory modeling of the single-particle phase function (backscattering region) cannot be excluded.

5.4 Large-scale surface roughness

The large-scale surface roughness is characterized by the $\bar{\theta}$ parameter which Hapke (Hapke, 1993) interprets an average slope of the surface structures. This is the only parameter that doesn't depend on wavelength in our fit procedure. To constrain it we performed fits of full-disk phase functions for each value of $\bar{\theta}$ in the range 10°-35° and chose the one that produced the smallest residual. We found a final value of $\bar{\theta}$=33° (we must point out that all the values above 30° gave similar fits). The result obtained seems too high if related to common slopes of craters and other topographic structures, and exceeds the values found by Domingue et al. (1995), while is close to the one found by Buratti (1985) for Mimas. Recent experimental analysis performed by Shepard and Helfenstein (2007), has shown that the value of $\bar{\theta}$ is not only affected by subpixel topography but also, and mainly, by roughness on the scale of particles clumping which can produce fairly high slopes, related to the angle of repose of the regolith, and consistent with our determination.

Typically, in phase function fit procedures, the estimated values of single-scattering albedo and surface roughness show a certain degree of correlation, which of course has no physical meaning and reveals a degeneration in the inversion process.

In our approach the evaluation of *w* comes from the spectral fit and it's completely independent on the determination of the roughness parameter, so the degree of degeneration of the regression is

606 reduced making the result more reliable. However, it must be noted, as pointed out in Davidsson et
607 al. (2009), that the treatment of surface roughness in Hapke's theory relies on the assumption of
608 "small mean slope" ($\bar{\theta}$ <10°), which allows to obtain analytical solutions. The value we retrieved
609 from the phase function analysis is far beyond this limit and must be considered with care.

610 Another issue is represented by the fact that in Hapke's theory multiple scattering between the
611 facets composing the surface is neglected which is not applicable for high albedo materials and
612 rough surfaces. In particular, icy surfaces have high albedo and, as shown in Shepard and
613 Helfenstein (2007), the sub-centimeters scale roughness implies fairly large slope angles (typically
614 above 10°).

615 This would limit the applicability of the roughness correction only to low albedo media, which is
616 not the case of icy surface, unless the analysis is restricted to wavelengths where strong absorption
617 bands are located (eg. 2.0 and 3.0 μm). In our analysis the derived $\bar{\theta}$ value produces good fits both
618 for high and low reflectance values (e.g. 1 and 2 μm). This would imply that the effect of multiple
619 scattering is less relevant than the "small mean slope" approximation.

620 **6. Feedback on the spectral fit**

621 The results of the phase function fits can be used to improve the spectral fit, which represented the
622 starting point of our analysis. The spectral fit, as explained in section 4.0, was performed assuming
623 an isotropic phase function and at phase angles large enough to avoid contributions from any OE.
624 Now, for each phase angle it is possible to compute the absolute spectrum, removing the
625 approximation of an isotropic single-particle phase function, including the OE and surface
626 roughness. We have recalculated the spectrum at $g=90°$, the one chosen to perform the starting
627 spectral fit, and plotted it in Fig. 11. The agreement between the fitted spectrum and the measured
628 one is almost perfect throughout the VIS-NIR region. Similar fits have been performed for each

629 spectrum (phase angle) of the dataset. As example the results relative to spectra at $g=2.1°$ and

630 $g=49.4°$ are plotted in Fig. 12.

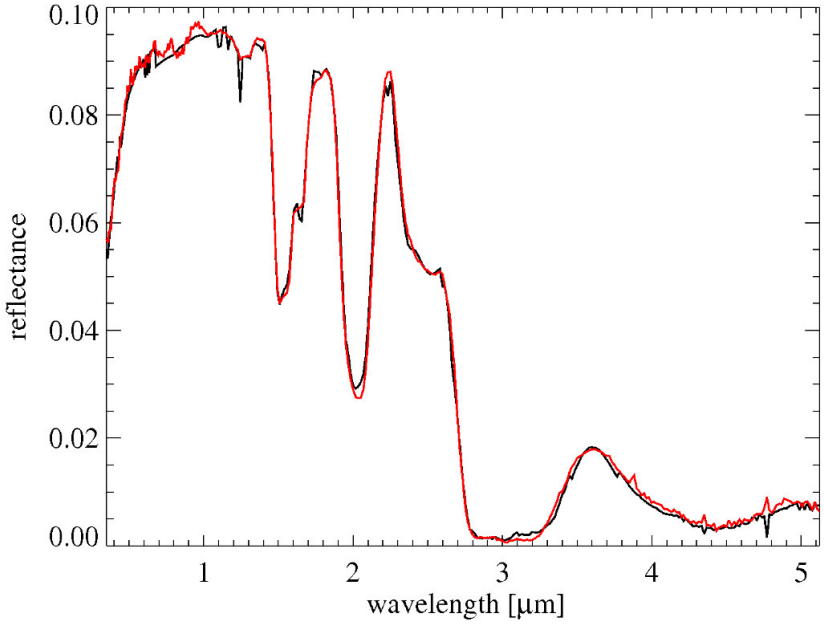

631

632 **[FIGURE 11]**

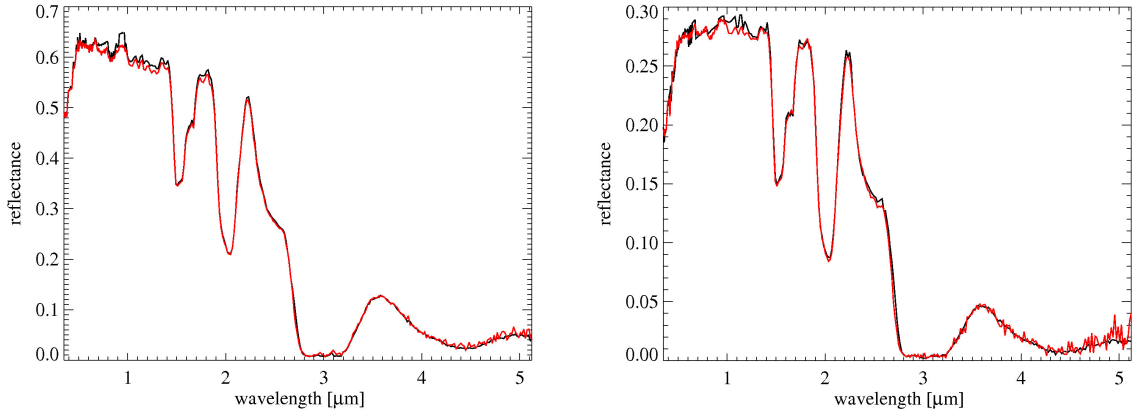

633

634 **[FIGURE 12]**

635

636

637 This high level of fit accuracy is possible because we deal with a large number of free parameters
638 and this allows us to tune the reflectance at each wavelength. This represents also the limitation of
639 this approach. In fact, any mismatches in the spectral fit due to grain size effects, as shown in
640 section 4.5 for the reflectances at 2.2μm and 3.1 μm, or due to an incomplete knowledge of the ice
641 optical constants, for instance, can be compensated by the contribution of the single-particle phase
642 function. The spectral fit will be optimal but we shall be misled in the interpretation of the
643 scattering mechanisms at work.

644 On the other hand, the trends observed in Fig. 8, 9 and 10 between phase curve parameters and the
645 single-scattering albedo points out some degree of physical correlation among those variables. For
646 instance, it is not totally unexpected to find that brighter surfaces have a narrower width of the
647 opposition effect than darker surfaces; the contribution of multiple scattering within the grains
648 attenuates the shadow hiding effect limiting it to a narrow region around the zero phase condition.
649 Also, for planetary surfaces, the slope of the linear part is larger for brighter surfaces and this is
650 consistent with the results shown in Fig. 8-9.

651 In other words, we could use these correlations to give preliminary estimates of the phase curve
652 parameters to be used in the determination of the spectral fit; this approach can prove valuable also
653 in case of incomplete or undersampled phase curves.

654

655 **7. Summary and conclusions**

656 We have studied surface spectrophotometric properties of Rhea, the largest icy satellite in the
657 saturnian system. The analysis has been performed on spectra acquired by VIMS onboard Cassini,
658 in the 0.35-5.12 μm spectral range, covering the 0.08°-110° phase angle interval. This approach
659 enabled us to investigate the compositional state of the ice covering the moon, the agglomeration
660 state of the medium and the roughness properties. Hapke's spectral and photometric model has been

661 used for the analysis. Four different organic compounds have been investigated as water ice
662 contaminants in order to model the reddening observed towards the UV. The best spectral fit in our
663 model is represented by an intraparticle mixture of crystalline water ice (99.6 %) and Triton tholin
664 (0.4%), with a grain size (diameter) of 38 μm. Major discrepancies between the measured and fitted
665 spectrum can be addressed to a grain size effect, because our particle diameter distribution
666 represents only the average size of the particles and therefore neglects the contribution of grains
667 with dimensions comparable to or less than the wavelength.

668 Once the composition of the particles in the model was frozen it was possible to investigate the
669 photometric properties of the satellite fitting the full-disk phase function at each wavelength. The
670 picture that emerges is that the dominating parameter in the scattering process is the single-
671 scattering albedo *w,* showing correlation with the single-particle phase function and OE. No
672 particular dependence of OE on wavelength was found, as expected, considering that the typical
673 grain size is larger than λ. The analysis of the OE indicates that both SH and CB are active, and
674 their relative contribution depend on the single scattering albedo value. Measuring the OE angular
675 width *h* in the SH regime we estimated a porosity varying between 65-77% .

676 The relatively high value of the roughness parameter ($\bar{\theta}$ =33°) is not compatible with the mean
677 slope of surface structures like craters, depressions or other reliefs. This points to a correlation of $\bar{\theta}$
678 with roughness on smaller scale, possibly on the order of centimeters, confirming the Shepard and
679 Helfenstein (2007) results, and providing an estimation of the regolith angle of repose.

680 The next step will be to apply the methodology described in this paper to the other full disk
681 observations of the Saturn's icy satellites. From this point of view the huge VIMS dataset represents
682 an extremely useful resource, given the large number of observations over a wide variety of
683 geometric conditions. Our goal will be to determine the distribution of contaminants in the saturnian
684 system and to point out compositional correlations among the moons. This analysis will represent a

685 useful tool for characterizing the effect of processes shaping the surfaces of these bodies:
686 interactions with other moons, with the rings, and with the saturnian magnetosphere, as well as the
687 surface activity of the moon itself.

688 As a future development we intend to investigate different kinds of grain size distributions
689 involving even smaller particles (e.g. as done by Clark et al., 2011b). This new approach is beyond
690 the limit of geometric optics applied in the present formulation of Hapke's model and requires to
691 use Mie theory (Mie, 1908) to compute single-scattering albedo of the particles.

692

693 Acknowledgments

694 The authors M.C., F.C., G.F., P.C., A.C. and F.T. acknowledge support from an Italian Space
695 Agency grant.The authors wish to thank the referees for their constructive comments.

696

697

698

699 APPENDIX: FIT PROCEDURE

700 Performing an inversion of a model with several free parameters is a challenging task. The most
701 common problem is to discriminate between different solutions that give similar results. Fitting
702 algorithms are able to find minima in the parameters space but it is difficult to discriminate between
703 local and absolute ones. To overcome this problem we adopted a very simple and transparent
704 method. We determined a grid in the parameter space through a quantization of the parameters over
705 the full range of variability. For each point of the grid (a single combination of the parameters) we
706 calculated the model prediction and compared it to the data. The best prediction represents the final

707 results of the fit. This method correctly finds the absolute minimum if the parameters space is
708 sufficiently sampled. The quantization we chose is related to the degree of precision needed by the
709 fit. At the same time the variability range for unbounded parameters has been fixed considering a
710 range of values with physical sense.

711 Concerning the spectral fit we chose a quantization for the particle diameter a_m of 1 μm in a range
712 extending from 10 to 100 μm; we knew from previous analysis that higher values where
713 unnecessary and that diameter values lower than 10 μm would have broken the limits given by
714 geometric optics in Hapke model. The water ice mixing percentage range changes corresponding to
715 the different mixtures, and in any case p was ≤ 1. The quantization "step" of the parameters has
716 been chosen as the minimum variation that could create an appreciable change in the output,
717 consequently the fitted value can be assumed with an uncertainty of half "step".

718 For the phase function fit the various parameters have been quantized in the following way:

719 $B_0 \in [0;2]$, $B_{0i} = i \cdot 0.1$, $i = 0,1,2,...,10$

720 $h \in [0.0001;0.1]$, $h_i = 10^{(-4+0.15 \cdot i)}$, $i = 0,1,2,\ldots,30$

721 $b \in [0;9]$, $b_i = i \cdot 0.1$, $i=0,1,2,\ldots,9$

722 $v \in [-1;1]$, $v_i = -1 + i \cdot 0.1$, $i = 0,1,2,\ldots,20$

723 $\bar{\theta} \in [10°;35°]$, $\bar{\theta}_i = i$, $i=10°,11°,12°,\ldots,35°$

724

725

Bibliography

Bowell, E., Hapke, B., Domingue, D., Lumme, K., Peltoniemi, J., Harris, A.W., 1989. Application of photometric models to asteroid. In: Binzel, R.P., Gehrels, T. and Matthews, M.S., (Eds.), Asteroids II, University of Arizona Press, Tucson, pp. 524–556.

Brown, R.H., Baines, K.H., Bellucci, G., Bibring, J.-P., Buratti, B.J., Capaccioni, F., Cerroni, P., Clark, R.N., Coradini, A., Cruikshank, D.P., Drossart, P., Formisano, V., Jaumann, R., Langevin, Y., Matson, D.L., McCord, T.B., Mennella, V., Miller, E., Nelson, R.M., Nicholson, P.D., Sicardy, B., Sotin, C., 2004. The Cassini Visual and Infrared Mapping Spectrometer (VIMS) investigation. Space Sci. Rev. 115 (1–4), 111–168.

Buratti, B.J., 1985. Application of a radiative transfer model to bright icy satellites. Icarus 61, 208-217.

Buratti, B.J., Hicks, M.D., 2003. The Dark side of Iapetus: A model that finally works? Bull. Am. Astron. Soc. 35, 915 (abstract).

Buratti, B.J., Mosher, J.A., Nicholson, P.D., McGhee, C.A., French, R.G., 1998. Near-infrared photometry of the saturnian satellites during ring plane crossing. Icarus 136, 223-231.

Buratti, B.J., Hicks, M.D., Soderblom, L.A., Britt, D., Oberst, J., Hillier, J.K., 2004. Deep space photometry of the nucleus of Comet 19P/Borrelly. Icarus 167, 16-29.

Ciarniello, M., Capaccioni, F., Filacchione, G., Coradini, A., Cerroni, P., Tosi, F., 2010a. VIS-IR spectral modeling of Rhea and Enceladus. EGU General Assembly 2010, 6177 (abstract).

Ciarniello, M., Capaccioni, F., Filacchione, G., Coradini, A., Cerroni, P., Tosi, F., Stephan, K., 2010b. Spectrophotometric analysis of Rhea surface scattering properties. Lunar Planet. Sci. XLI, 1643 (abstract).

Clark, R.N., Lucey, P.G., 1984. Spectral properties of ice-particulate mixtures and implications for remote sensing. I – Intimate mixtures. J. Geophys. Res.89, 6341-6348.

Clark, R.N., Owensby, P.D., 1981. The infrared spectrum of Rhea. Icarus 46, 354-360.

Clark, R.N., 1999, Chapter 1: Spectroscopy of Rocks and Minerals and Principles of Spectroscopy, *Manual of Remote Sensing*, (A.N. Rencz, ed.) John Wiley and Sons, New York, p 3-58, 1999. http://speclab.cr.usgs.gov/PAPERS.refl-mrs/refl4.html

Clark, R.N., Brown, R.H., Jaumann, R., Cruikshank, D.P., Buratti, B., Baines, K.H., Nelson, R.M., Nicholson, P.D., Moore, J.M., Curchin, J., Hoefen, T., and Stephan, K., 2008, Compositional mapping of Saturn's satellite Dione with Cassini VIMS and implications of dark material in the Saturn system, *Icarus*, 193, 372-386.

Clark, R. N., R. Carlson, W. Grundy, and K. Noll, 2011a, Observed Ices in the Solar System. In: Solar System Ices, Murthy Gudipati, ed., in press.

Clark, R. N., D. P. Cruikshank, R. Jaumann, R. H. Brown, J. M. Curchin, T. M. Hoefen, K. Stephan, C. M. Dalle Ore, B. J. Buratti, G. Filacchione, K. H. Baines, P. D. Nicholson, 2011b, The composition of Iapetus: Mapping Results from Cassini VIMS, *Icarus*, submitted.

Cruikshank, D.P., Roush, T.L., Bartholomew, M.J., Geballe, T.R., Pendleton, Y.J., White, S.M., Bell, J.F., Davies, J.K., Owen, T.C., de Bergh, C., Tholen, D.J., Bernstein, M.P., Brown, R.H., Tryka, K.A., Dalle Ore, C.M., 1998. The composition of Centaur 5145 Pholus. Icarus 135, 389-407.

764 Cruikshank, D.P., Dalle Ore, C.M., Roush, T.L., Geballe, T.R., Owen, T.C., de Bergh, C., Cash, M.D.,
765 Hartmann, W.K., 2001. Constraints on the composition of Trojan Asteroid 624 Hektor. Icarus 153, 348-360.

766 Cruikshank, D.P., Owen, T.C., Dalle Ore, C., Geballe, T.R., Roush, T.L., de-Bergh, C., Sandford, S.A.,
767 Poulet, F., Benedix, G.K., Emery, J.P., 2005. A spectroscopic study of the surfaces of Saturn's large
768 satellites: H_2O ice, tholins, and minor constituents. Icarus 175, 268–283.

769 Cuzzi, J., R. Clark, G. Filacchione, R. French, R. Johnson, E. Marouf, L. Spilker, 2009. Ring particle
770 composition and size distribution, In: *Saturn after Cassini/Huygens,* Springer, DOI 10.1007/978-1-4020-
771 9215-2, pp. 459-509

772 Cuzzi, J.N., J. A. Burns, S. Charnoz, R. N. Clark, J. E. Colwell, L. Dones, L. W. Esposito, G. Filacchione, R.
773 G. French, M. M. Hedman, S. Kempf, E. A. Marouf, C. D. Murray, P. D. Nicholson, C. C. Porco, J. Schmidt,
774 M. R. Showalter, L. J. Spilker, J. N. Spitale, R. Srama, M. Sremcevic, M. S. Tiscareno, J. Weiss, 2010. An
775 evolving view of Saturn's dynamic rings. *Science*, 327, 1470 - 1475.

776 Davidsson, B.J.R., Gutiérrez, P.J., Rickman, H., 2009. Physical properties of morphological units on Comet
777 9P/Tempel 1 derived from near-IR Deep Impact spectra. Icarus 201, 335-337.

778 Domingue, D., Verbiscer, A., 1997. Re-analysis of the solar phase curves of the icy Galilean satellites. Icarus
779 128, 49-74.

780 Domingue, D.L., Lockwood, G. and Thompson, D., 1995. Surface textural properties of icy satellites: A
781 comparison between Europa and Rhea. Icarus 115, 228-249.

782 Domingue, D.L., Denevi, B.W., Ernst, C.M., Holsclaw, G.M., Izenber, N.R., McClintock, W.E., Murchie,
783 S.L., Robinson, M.S., 2009. Regional color photometry of Mercury's surface. Lunar Planet. Sci. XL, 1301
784 (abstract).

785 Drossart, P. 1993. Optics on a fractal surface and the photometry of the regoliths. Planet. Space Sci. 41, 381–
786 393.

787 Emery, J.P., Burr, D.M., Cruikshank, D.P., Brown, R.H., Dalton, J. B., 2005. Near-infrared (0.8-4.0 μm)
788 spectroscopy of Mimas, Enceladus, Tethys, and Rhea. Astron. Astrophys. 435, 353-362.

789 Filacchione, G., Capaccioni, F., McCord, T.B., Coradini, A., Cerroni, P., Bellucci, G., Tosi, F., D'Aversa E.,
790 Formisano, V., Brown, R.H., Baines, K.H., Bibring, J.P., Buratti, B.J., Clark, R.N., Combes, M., Cruikshank,
791 D.P., Drossart, P., Jaumann, R., Langevin, Y., Matson, D.L., Mennella, V., Nelson, R.M., Nicholson, P.D.,
792 Sicardy, B., Sotin, C., Hansen, G., Hibbitts, K., Showalter, M., Newman, S., 2007. Saturn's icy satellites
793 investigated by Cassini-VIMS. I. Full-disk properties: 350-5100 nm reflectance spectra and phase curves.
794 Icarus 186, 259-290.

795 Filacchione, G., Capaccioni, F., Clark, R.N., Cuzzi, J.N., Cruikshank, D.P., Coradini, A., Cerroni,
796 P.,Nicholson, P.D., McCord, T.B., Brown, R.H., Buratti, B.J., Tosi, F., Nelson, R.M., Jaumann, R., Stephan
797 K., 2010. Saturn's icy satellites investigated by Cassini-VIMS. II. Results at the end of nominal mission.
798 Icarus 206 , 507-523.

799 Grundy, W.M., 2009. Is the missing ultra-red material colorless ice? Icarus 199, 560-563.

800 Hapke, B., 1993. Theory of Reflectance and Emittance Spectroscopy, Topics in remote sensing: 3,
801 Cambridge University Press, Cambridge, UK.

Hapke, B., 2002. Bidirectional reflectance spectroscopy. 5. The coherent backscatter opposition effect and anisotropic scattering. Icarus 157, 523-534.

Hapke, B., 2008. Bidirectional reflectance spectroscopy. 6. Effects of porosity. Icarus 195, 918-926.

Hapke, B., Nelson, R., Smythe, W., 1998. The opposition effect of the moon: Coherent backscatter and shadow hiding. Icarus 133, 89-97.

Hapke, B., Shepard, M.K, Nelson, R.M., Smythe, W.D., Piatek, J.,L., 2009. A quantitative test of the ability of models based on the equation of radiative transfer to predict the bidirectional reflectance of a well-characterized medium. Icarus 199, 210-218.

Hudson, R.S. and Ostro S.J., 1999. Physical model of Asteroid 1620 Geographos from radar and optical data. Icarus 140, 369-378.

Iess, L., Rappaport, N.J., Tortora, P., Lunine, J., Armstrong, J.W., Asmar, S.W., Somenzi, L., Zingoni, F., 2007. Gravity field and interior of Rhea from Cassini data analysis. Icarus, 190, 585-593.

Khare, B.N., Sagan, C., Arakawa, E.T., Suits, R., Callcot, T.A., Williams, M.W., 1984. Optical constants of organic tholins produced in a simulated titanian atmosphere: From soft X-ray to microwave frequencies. Icarus 60, 127–137.

Khare, B.N., Thompson, W.R., Cheng, L., Chyba, C., Sagan, C., Arakawa, E.T., Meisse, C., Tuminello, P.S., 1993. Production and optical constraints of ice tholin from charged particle irradiation of (1:6) C2H6/H2O at 77 K. Icarus 103, 290-300.

Lumme, K., and E. Bowell 1981. Radiative transfer in the surfaces of atmosphereless bodies. I. Theory. Astron. J. 86**,** 1694–1704.

MacKintosh, F.C., Sajeev, J., 1988. Coherent backscattering of light in the presence of time-reversal-noninvariant and parity-nonconserving media. Phys. Rev. B 37, 1884-1897.

Mallama, A., Wang, D., Howard, R.A., 2002. Photometry of Mercury from SOHO/LASCO and Earth. The phase function from 2 to 170 deg.. Icarus 155, 253-264.

Mallet, P., Guérin, C.A., Sentenac, A., 2005. Maxwell-Garnett mixing rule in the presence of multiple scattering: Derivation and accuracy. Phys. Rev. B 72, doi:10.1103/PhysRevB.72.014205

Mastrapa, R., Bernstein, M., Sandford, S., Roush, T., Cruikshank, D., Dalle Ore, C., 2008. Optical constants of amorphous and crystalline H2O-ice in the near infrared from 1.1 to 2.6 μm. Icarus 197 , 307-320.

Mastrapa, R.M., Sandford, S.A., Roush, T.L., Cruikshank, D.P., Dalle Ore, C.M., 2009. Optical constants of amorphous and crystalline H_2O-ice: 2.5-22 μm (4000-455 cm^{-1}) optical constants of H_2O-ice. Astrophysical Journal 701 , 1347-1356.

Maxwell-Garnett, J., 1904. Colours in metal glasses and in metallic films. Philosophical Transactions of the Royal Society of London. Series A 203 , 385-420.

McCord, T.B., Coradini, A., Hibbitts, C.A., Capaccioni, F., Hansen, G.B., Filacchione, G., Clark, R.N., Cerroni, P., Brown, R.H., Baines, K.H., Bellucci, G., Bibring, J.-P., Buratti, B.J., Bussoletti, E., Combes, M., Cruikshank, D.P., Drossart, P., Formisano, V., Jaumann, R., Langevin, Y., Matson, D.L., Nelson, R.M., Nicholson, P.D., Sicardy, B., Sotin, C., 2004. Cassini VIMS observations of the Galilean satellites including the VIMS calibration procedure. Icarus 172, 104-126.

McDonald, G.D., Thompson, W.R., Heinrich, M., Khare, B.N., Sagan, C., 1994. Chemical investigation of Titan and Triton tholins. Icarus 108, 137–145.

McGuire, A., F. and Hapke, B. W., 1995. An experimental investigation of light scattering by large, irregular particles. Icarus 113, 134-155.

Mie, G., 1908. Beiträge zur Optik trüber Medien, speziell kolloidaler Metallösungen. Ann. Phys. 330, 377

Miller, E., Klein, G., Juergens, D., Mehaffey, K., Oseas, J., Garcia, R., Giandomenico, A., Irigoyen, B., Hickok, R., Rosing, D., Sobel, H., Bruce, C., Flamini, E., DeVidi, R., Reininger, F., Dami, M., Soufflot, A., Langevin, Y., Huntzinger, G., 1996. The Visual and Infrared Mapping Spectrometer for Cassini. Proc. SPIE 2803, 206-220.

Pitman, K.M., Buratti, B.J., Mosher, J.A., 2010. Disk-integrated bolometric Bond albedos and rotational light curves of saturnian satellites from Cassini Visual and Infrared Mapping Spectrometer

Poulet, F., Cuzzi, J.N., Cruikshank, D.P., Roush, T.L., Dalle Ore, C.M., 2002. Comparison between the Shkuratov and Hapke scattering theories for solid planetary surfaces: Application to the surface composition of two Centaurs. Icarus 160, 313-324.

Poulet, F., Cruickshank, D.P., Cuzzi, J.N., Roush, T.L., French, R.G., 2003. Compositions of Saturn's rings A, B, and C from high resolution near-infrared spectroscopic observations Astron. Astrophys 412, 305-316.

Roush, T.L., 1994. Charon: More than water ice? Icarus 108 , 243-254.

Shepard, M.K., Helfenstein, P., 2007. A test of the Hapke photometric model. J. Geophys. Res. 112, doi: 10.1029/2005JE002625.

Shkuratov, Y., Starukhina, L., Hoffmann, H., Arnold, G., 1999a. A model of spectral albedo of particulate surfaces: Implications for optical properties of the Moon. Icarus 137, 245-246.

Shkuratov, Y., Kreslavsky, M.A., Ovcharenko, A.A., Stankevich, D.G., Zubko, E.S., Pieters, C., Arnold, G., 1999b. Opposition effect from Clementine data and mechanisms of backscatter. Icarus 141, 132-155.

Spencer, J.R., Denk, T., 2010. Formation of Iapetus' extreme albedo dichotomy by exogenically triggered thermal ice migration. Science 327, 432.

Thekaekara, M.P., 1973. Solar energy motion in space (SEMIS). In: Proc. Symp. Solar Radiation Meas. and Instrumentation, pp. 414–442. SEE N76-15973 06-92.

Thomas, P.C., Helfenstein, P., Veverka, J., Burns, J., Porco, C., Denk, T., Turtle, E., 2006. Sizes, shape, relaxation states and interior configurations of icy saturnian satellites. Bull. Am. Astron. Soc. 38, 621 (abstract).

Tosi, F., Turrini, D., Coradini, A., Filacchione, G., 2010. Probing the origin of the dark material on Iapetus. Mon. Not. R. Astron. Soc. 403, 1113-1130.

Verbiscer, A., and Veverka, J. 1989. Albedo dichotomy of Rhea: Hapke analysis of Voyager photometry. Icarus 82 , 336-353.

877 Warren, S.G., 1984. Optical constants of ice from the ultraviolet to the microwave. Applied Optics 23,1206-
878 1225.

879 Warrel, J. and Davidsson, B.J.R., 2010. A Hapke model implementation for compositional analysis of VNIR
880 spectra of Mercury. Icarus 209, 164-178.

881 Zubko, V.G., Mennella, V., Colangeli, L., Bussoletti, E., 1996. Optical constants of cosmic carbon analogue
882 grains – I. Simulation of clustering by a modified continuous distribution of ellipsoids. Mon. Not. R. Astron.
883 Soc. 282, 1321-1329.

884

885 **FIGURES CAPTIONS**

886 Figure 1. Schematic representations of two-components mixtures: areal (a), intimate (b) and
887 intraparticle (c). In a) the circle represents the field of view of the observing instrument, while in c)
888 the circle represents a single grain.

889

890 Figure 2. VIMS full-disk spectra of Rhea acquired at different phase angles, normalized at 1 μm.
891 An offset is added for clarity. The spectrum at each phase angle is compared to the spectrum at
892 *0.08°* (black curve). The leading fraction L.F. of each spectrum is reported.

893

894 Figure 3. Rhea's full-disk phase functions at various wavelengths. All the curves are normalized to
895 the value at minimum phase angle (0.08°).

896

897 Figure 4. Real part (*n*) of the refractive index for water ice and four organic contaminants:
898 hydrogenated amorphous carbon (ACH2), tholin from Khare et al. 1993, Titan tholin and Triton
899 tholin.

900

Figure 5. Imaginary part (*k*) of the refractive index for water ice and four organic contaminants: hydrogenated amorphous carbon (ACH2), tholin from Khare et al. 1993, Titan tholin and Triton tholin.

Figure 6. Simulated spectra of areal mixtures of water ice and ACH2 (left panel) and of water ice and Tholin from Khare et al.1993 (right panel). The percentage of water ice is indicated. Spectra are normalized at 1 µm. Grain size is 50 µm.

Figure 7. *Upper left panel:* areal mixture best fit. It is obtained with water ice and Titan tholin. The percentages of water ice (*p*) and contaminant (*pc*) and the grain size are indicated. Observed spectrum is in red. Spectra are normalized at 1 µm. *Upper right panel*: intimate mixture best fit. It is obtained with water ice and Titan tholin. The percentages of water ice (*p*) and contaminant (*pc*) and the grain size are indicated. Observed spectrum is in red. Spectra are normalized at 1 µm. *Bottom left panel:* Summary plot of intraparticle mixtures fits. Rhea spectrum is the continuum line. All the mixtures are water ice + contaminant. Spectra are normalized at 1µm. Grain sizes and compounds abundances are in Table 3. *Bottom right panel:* intraparticle mixture best fit. It is obtained with water ice and Triton tholin. The percentages of water ice *(p*) and contaminant (*pc*) and the grain size are indicated. Observed spectrum is in red. Spectra are normalized at 1 µm.

Figure 8. *Upper left panel*: phase function fit residuals at each wavelength against the single-scattering albedo. *Upper right panel:* single-particle phase function at 20° and 90° ratio for each wavelength against the single-scattering albedo. *Bottom left panel:* opposition effect width against

924 the single-scattering albedo. *Bottom right panel:* opposition effect amplitude against the single-
925 scattering albedo.

926

927 Figure 9. Rhea full-disk phase functions at wavelengths relative to increasing value of the single-
928 scattering albedo. Single-scattering albedo values and corresponding wavelengths are indicated.
929 Curves are normalized at minimum phase angle (0.08°).

930

931 Figure 10. Distribution of fitted *b* (left panel) and *v* (right panel) values respect to the single
932 scattering albedo. *N* represents how many times a certain value of the parameter is obtained in a
933 given range of *w* values. The *w* range (0-1) is divided in intervals 0.1 wide.

934

935 Figure 11. Final absolute spectral fit at $g = 90.2°$ ($p = 0.996$, $pc = 0.004$, $a_m = 38\ \mu m$, intraparticle
936 mixture). Isotropic single-particle phase function approximation has been removed and the
937 correction due to roughness has been introduced. Observed spectrum is red.

938

939 Figure 12. *Left panel*: final absolute spectral fit at $g = 2.1°$. *Right panel*: final absolute spectral fit at
940 $g = 49.4°$. The two simulations are obtained with an intraparticle mixture ($p = 0.996$, $pc = 0.004$, a_m
941 $= 38\ \mu m$). Isotropic single-particle phase function approximation has been removed and the
942 correction due to roughness has been introduced. Observed spectrum is red.

943

944

945

946
947
948 Highlights
949 >Rhea's spectrum and phase function modeling. >Spectra from VIMS on board
950 Cassini spacecraft. >Intraparticle mixture of water ice and Triton tholin reproduces
951 observed reddening. >Determination of phase function parameters. >Dependence
952 of phase function parameters on single scattering albedo.

953